

Analysis of a two-dimensional photonic bandgap structure fabricated by an interferometric lithographic system

Cheng-Wei Chien,¹ Yun-Chih Lee,² Po-Shen Lee,² Jenq-Yang Chang,² and Jyh-Chen Chen^{1,*}

¹Department of Mechanical Engineering, National Central University, Jhongli 32001, Taiwan

²Department of Optics and Photonics, National Central University, Jhongli 32001, Taiwan

*Corresponding author: jcchen@cc.ncu.edu.tw

Received 27 November 2006; revised 26 January 2007; accepted 30 January 2007;
posted 31 January 2007 (Doc. ID 77317); published 15 May 2007

An interferometric lithographic technique and double exposure method are applied to theoretically and experimentally investigate several kinds of 2D periodic structures. The shape, lattice symmetries, and lattice constants of the 2D structures, for different substrate rotational angles, are obtained from the simulated predictions. The shape of the 2D structures can be varied by controlling the rotational angle of the substrate and the development process, and they are validated experimentally. The variation of the lattice symmetry of the 2D structure with the substrate rotational angle is discussed in detail in relation to the axial angle and lattice constant. It is found that square, circular, rectangular, and elliptical scatterers which are arranged in parallelogram, triangular, and square lattices (with different lattice constants) can be obtained. The photonic bandgaps for each condition are also investigated. When the substrate rotational angles are the same, the normalized frequency ($\omega a/2\pi c$) of photonic bandgap structures with an equal filling factor are very similar regardless of the interference angle. The results are helpful in designing the forbidden frequency when the lattice constant and the scatterer shape can be controlled by the interferometric lithographic technique. © 2007 Optical Society of America

OCIS codes: 260.3160, 220.4000.

1. Introduction

Interferometric lithography is one of the most important and widely studied types of lithographic system being developed today; it is suited for the construction of 1D, 2D, and 3D periodic structures of different dimensions and with a large area [1–3]. These periodic structures can be applied not only to the fabrication of photonic crystals (PCs), waveguides, and cavity resonators [4–6] but can also be used to enhance the hydrophobic behavior of nonwetting surfaces [7,8]. It is well known that the photonic bandgap (PBG) is the major feature requiring attention in the application of the PCs. The propagation of electromagnetic waves of certain frequencies within the PBG is prohibited, regardless of their polarization and propagation direction. However, the PC [9,10] simulation results show that the PBG is strongly affected by the lattice symmetry as well as the shape,

orientation, and size of the scatterers. Although electron beam lithography [11,12] because of its high resolution and flexibility in constructing arbitrary patterns is largely employed to fabricate PBG structures, it requires expensive equipment and is time consuming. The interferometric lithographic system because of its repeatability, rapidity, and high resolution, is acknowledged to be a powerful tool for fabricating PBG structures. With this system and utilizing the double exposure method [2,3], 2D intensity patterns are obtained by superposing a pair of 1D interference fringes. The included angles between each 1D interference fringe are selected to obtain different kinds of 2D intensity pattern. From their results, we can conjecture that the geometry, lattice symmetry, and lattice constant of the scatterers can be easily controlled by altering the interference angle and substrate rotational angle. However, in most past studies the concern has been how to employ this technique to fabricate triangular and square lattices with air holes in a dielectric material [13], triangular lattices with circular or elliptical air holes [14], or to

create periodic structures with complicated geometries by changing the phase between the interfering beams [15]. When the lattice is not triangular or square, that is, when the substrate rotational angle is not 60° or 90° , the properties of the lattice symmetry, lattice constant, and PBG as substrate rotational angles from 15° to 80° have been less investigated. To design a PBG for a desired region of the electromagnetic spectrum, it is important to have comprehensive knowledge of the PBG structures, which can be constructed by the interferometric lithographic technique.

To minimize expensive replication during actual manufacturing trials, before applying the interferometric lithography system to fabricate periodic structures, simulation analysis has been recognized as an economic and useful tool for understanding and predicting how a process will proceed. Numerous 1D and 2D interferometric models have been developed [16–18]. However, in most of the current exposure models of laser interferometric lithographic techniques, the emphasis is placed on the interference part, especially the phase difference between the interference beams. However, the overall effects, such as the Gaussian intensity distribution and the intensity decay caused by the stretch in area of different interference angles within the whole exposure area, have recently been considered by Chien *et al.* [19].

Since the scatterer's shape varies with the substrate rotational angle but is the same throughout the whole exposure area, the difference between scatterers at different positions within the exposure area is only the exposure dose, which is caused by Gaussian intensity distribution. Therefore, in this study we apply the Chien *et al.* [19] interferometric exposure model but use the localized normalization intensity. We focus on investigating variations in the 2D intensity arrays under different conditions. The shape of the scatterers is studied by altering the substrate rotation angle from 15° to 90° and by controlling the development process as well. As the substrate rotational angle increases from 15° to 90° the lattice symmetries and lattice constants are investigated via the simulations of the isointensity surface. The plane wave expansion method is commonly used in calculating the PBG. Quinonez *et al.* [14] and Leung and Liu [20] employed the plane wave expansion method to analyze the photonic bandgap for elliptical and circular air holes in a hexagonal lattice and elliptical air holes in a rectangular lattice, respectively. Ho *et al.* [21] utilized this method to analyze the photonic bandgap for dielectric spheres in a cubic lattice. Here, corresponding to realizable structures produced by the interferometric lithographic system, the plane wave expansion method is applied to analyze the PBG of these structures by solving Maxwell's equations [22,23].

2. Experimental Procedure

The arrangement of the interferometric lithographic system utilized for patterning the periodic structure

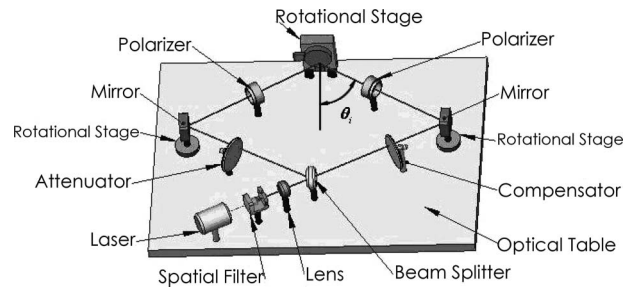


Fig. 1. (Color online) Schematic experimental arrangement of the interferometric lithographic system.

in the photoresist is depicted in Fig. 1. A He–Cd laser (wavelength of 441.6 nm, maximum power of 50 mW, coherent length of 10 cm) acts as the exposure light source. The laser beam passes through a beam expander consisting of a spatial filter and a collimation lens and is to be expanded to a diameter of 5 mm. The beam is then divided into two beams by a broadband, nonpolarizing cubic beam splitter. The polarizer is used to ensure that the two beams have the same direction of polarization. To ensure that the two beams are equal in intensity and have an equal optical path length, an attenuator is placed on one arm and a compensator on the other. In this way the best fringe contrast can be obtained. Only the TE mode is used in this study. For sample preparation, a silicon substrate is coated with photoresist. After this, the sample is mounted on a rotational stage for multitime exposure. The samples are spin coated with a Shipley S1813 at the maximum spinning speed of 2500 rpm and finally baked at 115°C for 120 s to remove the solvent in the photoresist. The thickness of the photoresist after all these steps is measured by Dektak and is found to be approximately $1.5\ \mu\text{m}$ thick. The interference angles θ_i of two coherent beams are made to overlap to form an interference pattern in the photoresist by operating two rotational mirrors. After exposure, the samples are developed in a Microposit MF-321 developer diluted with 1:4 deionized water, then hard baked at 130°C for 100 s. A periodic photoresist structure on the silicon substrate is obtained.

3. Simulation Models

A. Exposure Model

The laser light source used in the present interferometric lithographic system has a Gaussian distribution. The electric field of a large size laser beam can be expressed as follows:

$$\vec{E}(x, y, z) = E_0 \times \exp\left[-\frac{r^2}{w_0^2}\right] \times \exp - i(\vec{k}\vec{r}_k), \quad (1)$$

$$r = \sqrt{x^2 + y^2}, \quad (2)$$

where \vec{r}_k is the position vector, E_0 is the amplitude, w_0 represents the beam radius, r is the position within

the beam, \vec{k} is the propagation vector of the wave, and $i = \sqrt{-1}$. In the interferometric lithographic technique, the TE mode is usually selected. Theoretically, the intensity distribution of interference I can be expressed as the time average of the magnitude of the electric field intensity squared, shown as

$$I = \langle |\vec{E}_1 + \vec{E}_2|^2 \rangle_t, \quad (3)$$

where \vec{E}_1 and \vec{E}_2 are the electric fields of the interference beams. The interference intensity is coupled with a Gaussian distribution of I . The beam deformation caused by differences in the incident angle at the exposure surface can be derived to be [15]

$$I = (I_{01} + I_{02}) \left[1 + V \cos\left(\frac{2\pi}{P} x\right) \right] \times \exp\left[-2\left(\frac{x^2}{w_{0x}^2 \sec^2 \theta_i} + \frac{y^2}{w_{0y}^2} \right) \right], \quad (4)$$

where w_{0x} and w_{0y} represent the beam size along the x and y directions, I_{01} , I_{02} represent the central maximum light intensities of the two interference beams, considering the Fresnel reflection on the air-photoresist interface, V is the visibility of the interference fringe, θ_i is the interference angle, and P is the interference period given by

$$P = \frac{\lambda}{2 \sin \theta_i}, \quad (5)$$

where λ is the wavelength of the light source. For multiexposures, the final intensity can be expressed as

$$I_{ME} = \sum_l I_{\Phi_l}, \quad (6)$$

where l is the exposure sequence at the substrate rotational angle of Φ .

B. Plane Wave Expansion Method

We use the plane wave expansion method to analyze the photonic bandgap of our structure by solving Maxwell's equation. In terms of the magnetic field H , Maxwell's equation becomes

$$\nabla \times \left[\frac{1}{\varepsilon(r)} \nabla \times H \right] = \frac{\omega^2}{c^2} H, \quad (7)$$

where $\varepsilon(r)$ is a position-dependent dielectric constant; r lies in the plane normal to the rods; ω is the frequency; and c is the speed of light in vacuum. Expanding the magnetic field $H(r)$ and the dielectric function $\varepsilon(r)$ in a series of plane waves, we obtain

$$H(r) = \sum_G \sum_{j=1,2} H_{G,j} \hat{e}_j \exp i(k + G)r, \quad (8)$$

$$\varepsilon(r) = \sum_G \varepsilon(G) \exp i(Gr), \quad (9)$$

where k is the wave vector in the first Brillouin zone, G is a reciprocal-lattice vector, and \hat{e}_j ($j = 1, 2$) are unit vectors orthogonal to $(k + G)$. The Fourier coefficient $\varepsilon(G)$ is defined by

$$\varepsilon(G) = \frac{1}{S} \int_S \varepsilon(r) \exp[-i(G \cdot r)] dr,$$

where the integration is carried out over area S of one unit cell of the lattice. Two standard eigenvalue equations are obtained by substituting Eqs. (8) and (9) into Eq. (7), corresponding to two independent polarizations. Here the equation for the E polarization mode with the electric field parallel to the rod is given by

$$\sum_{G'} |k + G| |k + G'| \varepsilon^{-1}(G - G') H_{G',1} = \frac{\omega^2}{c^2} H_{G,1}. \quad (10)$$

Equation (10) can be solved numerically.

4. Results and Discussions

In the simulation an isointensity surface is first developed by superposing a pair of 1D interference fringes of the same intensity but different rotational angles of $\Phi_1 = 0^\circ$ and $\Phi_2 = 15^\circ, 50^\circ$, and 90° , respectively, as depicted in Fig. 2. The higher intensity areas (red regions) represent the parts that experience greater exposure energy, while the lower intensity parts (blue regions) experience less exposure energy. When positive photoresist is used for exposure, the photoresist in the lower intensity parts will be retained (photoresist structure) after the development process. It can easily be seen that the arrays gradually become smaller, and their shape varies from longer to shorter rectangles and finally to squares as the rotational angle of the substrate increases from 15° to 90° . In Figs. 2(a) and 2(b) it can be clearly seen that the cross sections of the isointensity surface are rectangles then evolve to ellipses in shape. Similarly, in Fig. 2(c), the isointensity surfaces are squares and then evolve to circles in shape. This implies that when we fabricate PBG structures, the shapes of the scatterers can easily be varied by altering the exposure conditions and the development process.

Structures corresponding to the simulation results are now constructed experimentally. Figure 3 shows scanning electron microscopic (SEM) images of 2D periodic structures with different rotational angles taken after the second exposure step. The average exposure energy of a single beam is approximately 100 mJ/cm^2 . The interference angles, as shown in Figs. 3(a), 3(b), and 3(c), are nearly 10° . The pits (darker parts) in Figs. 3(a), 3(b), and 3(c) are larger than the structures that should be retained after development (lighter parts). This phenomenon is caused by overdevelopment. When the rotation angle of Φ_2 increases to $15^\circ, 50^\circ$, and 90° , the respective aspect ratio becomes approximately 8.17 and 3.67 and finally 1. The arrangement of the pits and islands

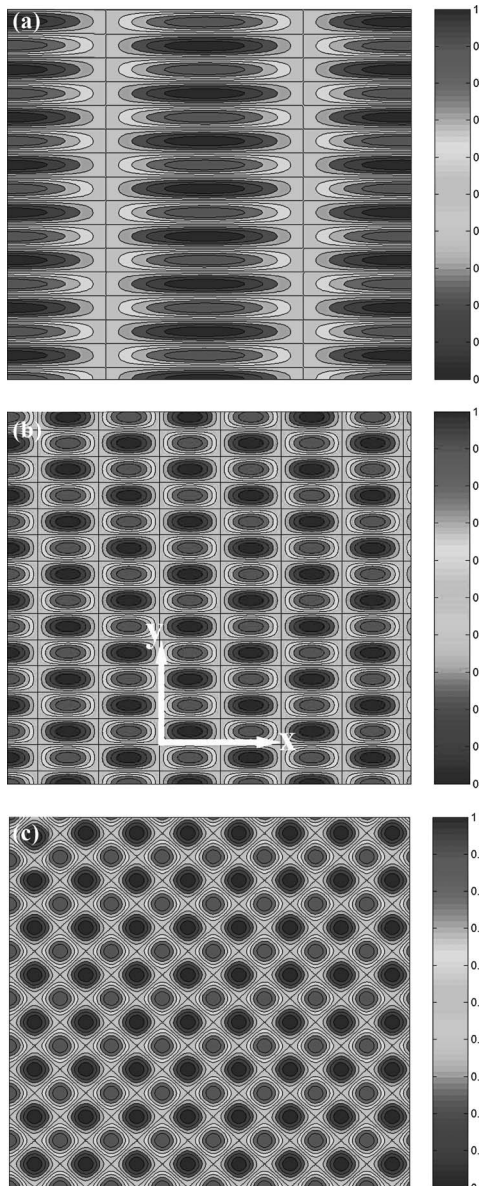


Fig. 2. (Color online) Normalized isointensity surface of the 2D simulation results superposed by a pair of 1D interference fringes with intensities of $I_{01} = I_{02} = I$ and $\Phi_2 =$ (a) 15° , (b) 50° , (c) 90° .

forms a parallelogram lattice when the rotational angle is $\Phi_2 = 50^\circ$, but forms a square lattice shape when the rotational angle is $\Phi_2 = 90^\circ$. The rippled sides around the pits and inside the structures (lighter parts) obtained when a high refractive index material is used as a substrate are caused by the standing wave effect. This standing wave effect is helpful in investigating the shape of the structure retained after development. We increase the development time of the two cases, $\Phi_2 = 50^\circ$ and 90° , to obtain another kind of structure. Figure 4 shows SEM images of the 2D periodic structures obtained under the same exposure conditions as in Figs. 3(b) and 3(c) but with different development times. When the development time increases to 13 s, the connecting structures in Fig. 3(b) are partially removed and the

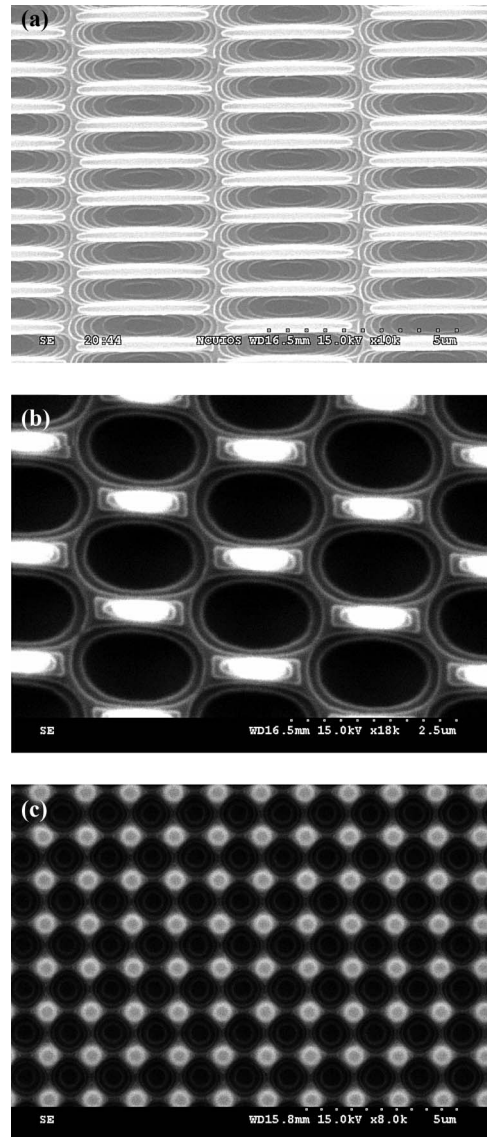


Fig. 3. Two-dimensional periodic structures at rotational angles of $\Phi_1 = 0^\circ$ and $\Phi_2 =$ (a) 15° , (b) 50° , (c) 90° under the same exposure energy per step and a 10 s development time at room temperature.

retained structures become rectangular in shape and are arranged in a parallelogram lattice. When the development time increases to 18 s, the connected structures in Fig. 3(c) are totally washed out, and the retained structures become smooth dots with a diameter of $0.58 \mu\text{m}$ arranged in a square lattice. The nonlinearity and rate of the isotropic wet development need to be noticed during the development process. The geometries of rectangular and square scatterers will develop rapidly to circular or elliptical structures. The remaining photoresist over the corners of the squared or rectangular structures will also be thin. When the entire development process is unstable, strong process errors (low repeatability and variations of the geometries of the structures along the sample) will occur. Therefore the development process needs to be investigated in detail. Mello *et al.* [24] obtained experimentally the relation between the pho-

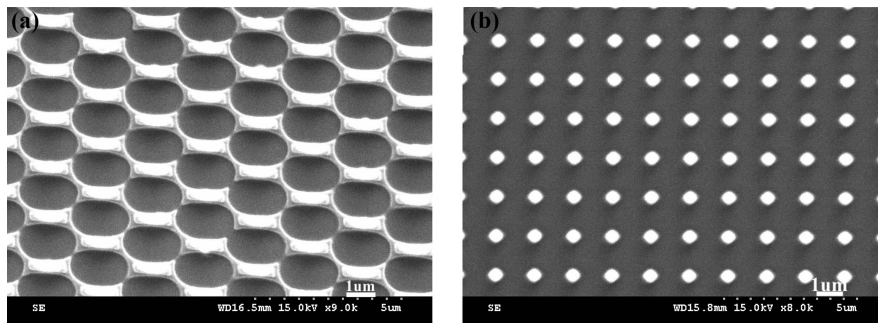


Fig. 4. Two-dimensional periodic structures given the same exposure energy per step at rotational angles of $\Phi_1 = 0^\circ$, and (a) $\Phi_2 = 50^\circ$ and a 13 s development time at room temperature, (b) $\Phi_2 = 90^\circ$ and a 18 s development time at room temperature.

toresist solubility rates and the exposure energy for different developer's concentrations. They also discussed the nonlinearity of the photoresist response. The relation included the overall response during the experimental procedures, such as the development concentration, temperature, prebake conditions, and nonlinearities introduced by the development process that should be obtained before carrying on the development process. It is also the case that structures with thin corners are unsuitable for pattern transference using wet etching. Instead, a high selectivity ion coupled plasma dry etching system should be used for pattern transforming. Keeping the entire process stable so as to minimize the process errors is the most important thing. When the aforementioned issues are overcome and the whole process handled stably, it should be possible to construct 2D structures of specified dimensions by controlling the development process.

In addition, the scatterers of photonic bandgap structures can be either dielectric rods in air or air rods in dielectric media. The aforementioned exposure conditions are suited only to construct rods in air. By decreasing the exposure dose, we can obtain air rods in the photoresist, as shown in Fig. 5.

The period is one of the factors of most concern in periodic structures. The period of 1D interference

fringes can be easily obtained via Eq. (5), but the period of 2D periodic structures is difficult to describe, especially when the periodic structures are distorted asymmetrically with the substrate rotational angles. Therefore we classify the period in two specific directions, as shown in Fig. 2(b). For convenience, the period in the x direction is called the long side and that in the y direction the short side. The periods along the two directions of the 2D structure are influenced by the interference angle and the difference between the substrate rotational angles of each step ($\Delta\Phi = |\Phi_2 - \Phi_1|$). Here, to eliminate the influence of the interference angles on the period of the 2D structure we define the normalized period (NP) as

$$NP_{Long} = \frac{\text{Long side Period}}{P}, \quad (11)$$

$$NP_{Short} = \frac{\text{Short side Period}}{P}. \quad (12)$$

Figure 6 shows the simulated and experimental results of the normalized periods for the long and short sides with different substrate rotational angles. In

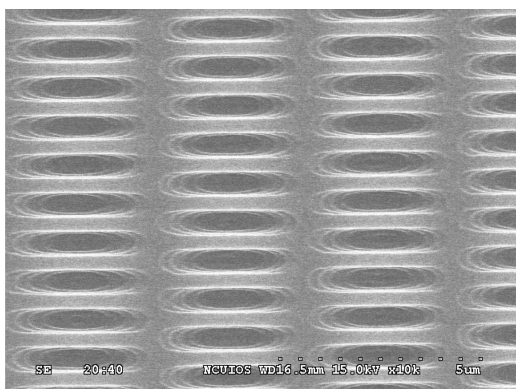


Fig. 5. Two-dimensional air rods in photoresist at rotational angles of $\Phi_1 = 0^\circ$ and $\Phi_2 = 15^\circ$, an average exposure energy of 10 mJ/cm^2 for a single beam, and a 10 s development time, at room temperature.

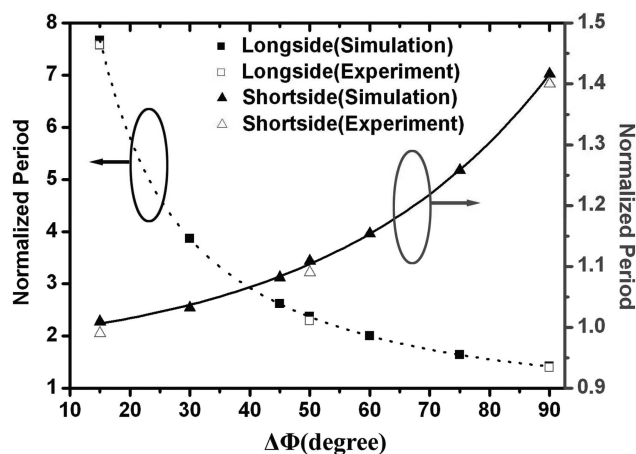


Fig. 6. (Color online) Normalized long and short side period simulation results at different $\Delta\Phi$.

Table 1. Constant Values of the Parameters in the Normalized Period Equation

Parameters	Values	Parameters	Values
P_{L0}	1.02	P_{S1}	0.04
P_{L1}	2.96	F_{L1}	34.15
P_{L2}	2.92	F_{L2}	32.28
P_{L3}	18.37	F_L	8.12
P_{S0}	0.95	F_{S1}	36.28

the simulation, the difference between the normalized period of the long and short sides is large when the rotational angle is low (the period of the long side is approximately 7.6 times larger than the period of short side at a rotational angle of 15°), but decreases as the rotational angle increases. The dashed and solid curves indicate the fitted third-order exponential decay and a one-order exponential growth function, respectively. We next obtain the relationship between the normalized period NP_{Long} , NP_{Short} , and the difference between the substrate rotational angles of each step $\Delta\Phi$ for a 2D structure:

$$NP_{Long} = P_{L1} \exp\left(\frac{-\Delta\Phi}{F_{L1}}\right) + P_{L2} \exp\left(\frac{-\Delta\Phi}{F_{L2}}\right) + P_{L3} \exp\left(\frac{-\Delta\Phi}{F_{L3}}\right) + P_{L0}, \quad (13)$$

$$NP_{Short} = P_{S1} \exp\left(\frac{\Delta\Phi}{F_{S1}}\right) + P_{S0}, \quad (14)$$

where P_{L0} , P_{L1} , P_{L2} , P_{L3} , P_{S0} , P_{S1} , F_{L1} , F_{L2} , F_{L3} , and F_{S1} are all constants; the value of each parameter is listed in Table 1. By multiplying Eqs. (13) and (14) by P , the period of the 2D structure at any interference angle along the two directions can be entirely predicted. The simulated results closely match the experimental ones, as can be seen in Fig. 3. It can be verified that 2D structures with similar dimensions but different periods can be constructed via the assistance of these predictions and a well-controlled development process.

The symmetry and lattice constants play an important role in PBG structures. Hence we simulate the lattices of scatterers with different rotational angles, as shown in Fig. 7. An obviously square lattice, which can be seen in Fig. 7(c), forms when $\Delta\Phi = 90^\circ$. When $\Delta\Phi = 60^\circ$ [Fig. 7(b)], the axial angle (θ_L) between lattice constants a and b equals 60° , and the scatterers are arranged in a triangular lattice. Figure 8 shows the simulation results for the relationship between θ_L and $\Delta\Phi$. The axial angle increases linearly from 50° to 85° as $\Delta\Phi$ decreases from 80° to 10° . Lattice constants a and b also vary with the $\Delta\Phi$. As mentioned above, the lattice constant of a equals the period of the short side, and the lattice constant of b can be expressed as

$$b = \frac{1}{2} a \times \sec \theta_L, \quad (15)$$

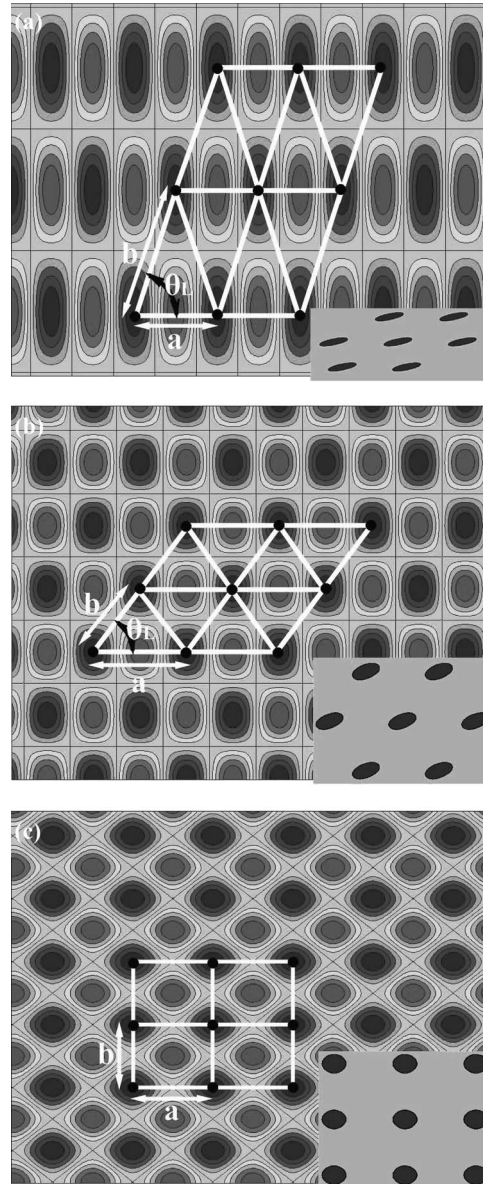


Fig. 7. (Color online) Scattering lattice at $\Delta\Phi =$ (a) 30° (parallelogram), (b) 60° (triangular), (c) 90° (square).

where $a = P \times NP_{Short}$. Here we briefly discuss the shape and lattices of the scatterers, which can be constructed by the interferometric lithographic system. Square and triangular lattices are formed when $\Delta\Phi$ equals 90° and 60° , respectively. The shape of the scatterers varies from square to round and from rectangular to elliptical when $\Delta\Phi$ equals 90° and 60° , respectively. When the angles of $\Delta\Phi$ differ from 60° and 90° , parallelogram lattices are constructed; these can be described in detail from the lattice constants and axial angles. The shape of the scatterers varies from rectangular to elliptical.

Corresponding to the structures realizable in an interferometric lithographic system, three types of lattice and four different shapes of dielectric medium are analyzed: parallelogram [25], triangular and square lattices, rectangular and elliptic for parallel-

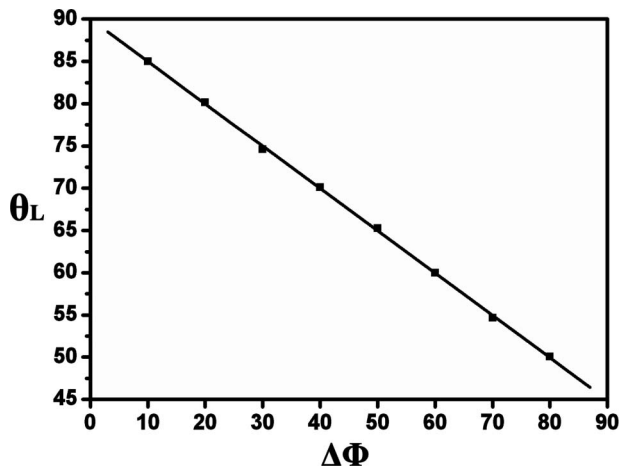


Fig. 8. Simulation axial angle results θ_L at different $\Delta\Phi$ angles.

ogram and triangular lattices, and square and circular for square lattice. The plane wave expansion method is used to analyze the PBG of our structure by solving Maxwell's equations. The refractive indices of the dielectric media and air are 3.48 (silicon) and 1, respectively. The lattice constants for each lattice are denoted as a and b and are shown in Fig. 7. They can be calculated via Eqs. (13)–(15); detailed values are given in Table 2. Here we choose 0.4 times the long and short side period as the length and width of the rectangular scatterers. Similarly, we select 0.125 times the long and short side period as the major and minor axes of the elliptic scatterers. The dielectric rods in air with different shapes are analyzed for each type of lattice.

The results for a parallelogram lattice with an interference angle of 30° are presented first. The gap–midgap ratio [26] $\omega_R \equiv \Delta\omega/\omega_g$ (where ω_g is the

frequency at the middle of the gap, and $\Delta\omega$ is the frequency width of the gap) and the filling factor f for different rotation angles are discussed. When $\Delta\Phi = 60^\circ$, the PBG structure consisting of rectangular rods arranged in a triangular lattice with $f = 0.319$ is examined. The frequency at the middle of the gap is $\omega_g = 0.255$, and the frequency width is $\Delta\omega = 0.06$ and results in the largest gap–midgap ratio of $\omega_R = 23.5\%$. The full-zone band structure is shown in Fig. 9(a), and the bandgap is indicated by the oblique lined area. By increasing the development time, an elliptic PBG rod structure is obtained with $f = 0.024$ and $\omega_R = 22.7\%$. When $\Delta\Phi = 50^\circ$, $f = 0.024$ and 0.318 for elliptic and rectangular rods, their gap–midgap ratios are 10.5% and 10.1% , respectively, which is approximately one half of that of the 60° case. However, when $\Delta\Phi = 15^\circ$ the scatterers are elliptical in shape, and there is no gap in this kind of PBG structure. The rotational angles of $\Delta\Phi = 15^\circ$, 50° , and 60° are considered here. Regardless of the shape of the scatterers, the largest PBG appears in the triangular lattice, i.e., $\Delta\Phi = 60^\circ$. Next, a parallelogram lattice with an interference angle of 10° is considered. The substrate rotation angles = 15° , 50° , and 60° and PBG structures with two shapes are also investigated. When $\Delta\Phi = 60^\circ$, the PBG structure consisting of rectangular rods arranged in a triangular lattice with $f = 0.318$ is examined. The frequency at the middle of the gap is $\omega_g = 0.255$, and the frequency width is $\Delta\omega = 0.06$, while the largest gap–midgap ratio is $\omega_R = 23.5\%$. The full zone of the band structure is shown in Fig. 9(b) and the bandgap is indicated by the oblique lined area. The results are almost the same as in cases where the interference angle is 30° . When there are two different interference angles, 10° and 30° , at $\Delta\Phi = 60^\circ$ different lattice constants will be obtained; i.e., $0.512 \mu\text{m}$ for 30° and

Table 2. Properties of the PBG Structures Under Different Substrate Rotational Angles

Interference Angle	Lattice Type	Scatterers	$\Delta\Phi$	a	b	f	ω_g	ω_R
10	Parallelogram	Rectangle	15	1286	4874	0.317	0.289	0.028
			50	1413	1672	0.318	0.219	0.107
	Triangular	Parallelogram	60	1477		0.318	0.255	0.235
			15	1286	4874	0.024	x	x
	Parallelogram	Ellipsoid	50	1413	1672	0.024	0.437	0.107
			60	1477		0.024	0.512	0.228
	Triangular	Square	60	1477		0.160	0.323	0.362
	Square	Circle	90	1795		0.049	0.425	0.289
30	Parallelogram	Rectangle	15	447	1711	0.320	0.289	0.028
			50	400	580	0.318	0.219	0.101
	Triangular	Parallelogram	60	512		0.319	0.255	0.235
			15	447	1711	0.024	x	x
	Parallelogram	Ellipsoid	50	400	580	0.024	0.438	0.105
			60	512		0.024	0.512	0.227
	Triangular	Square	60	512		0.159	0.323	0.362
	Square	Circle	90	623		0.050	0.425	0.288

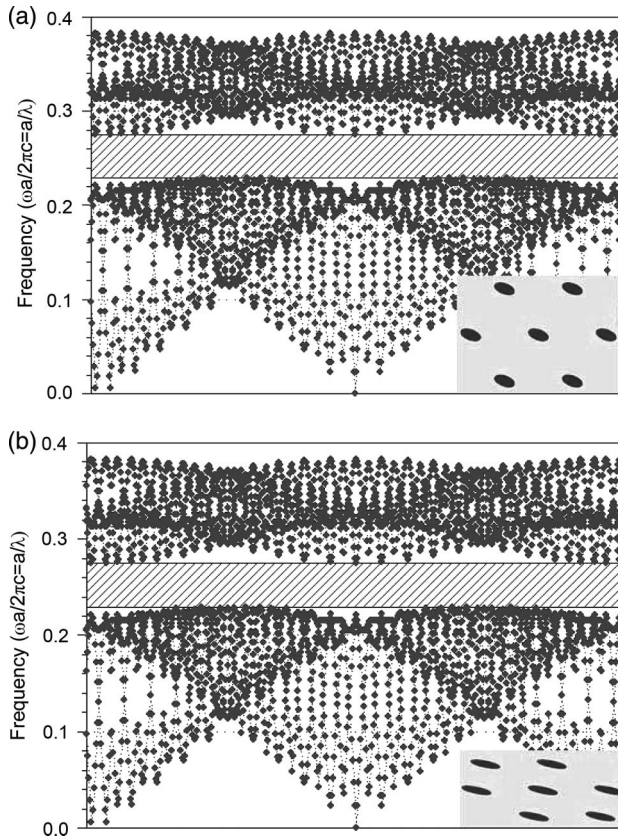


Fig. 9. (Color online) Photonic band structure of H polarization for triangular rods in air, when $\Delta\Phi = 60^\circ$ and $f = 0.024$, at an interference angle of (a) 30° and (b) 10° .

$1.477\ \mu\text{m}$ for 10° . Such results are helpful in the design of forbidden frequencies when the lattice constant can be controlled by our interferometric lithographic technique. In other words, a certain forbidden bandgap can be generated by controlling the interference angle to prohibit a specific frequency of electromagnetic wave from propagating within the PBG structure. All these results are shown in Table 2.

To reveal the correlation between the ω_R and the filling factor f , we analyze each ω_R , while making changes in the size of the elliptic rods; the interference angle is 30° . The filling factor increases from 0.02 to 0.3. The relationship between ω_R and f at different $\Delta\Phi$ is shown in Fig. 10. As f increases, the ω_R increases until it reaches a peak value, then decreases, which coincides with the results of other researchers [9,27] under a similar structural configuration. When the substrate rotation angle rises from 30° to 60° , the maximum ω_R moves to higher f but with decreasing value. The maximum ω_R occurs at 70° . When the substrate rotation angle is greater than 30° , the largest ω_R occur at approximately $f = 0.1$. According to the correlation between f and ω_R , and the value of ω_g , the desired bandgap can be selected, and the largest frequency width can also be obtained by selecting the proper filling factor. Last, the PBG structures with square lattice are studied. When $\Delta\Phi = 90^\circ$ the dielectric rods are square and

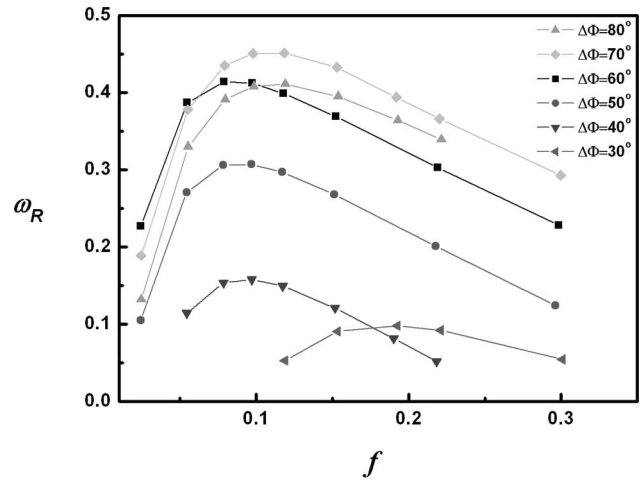


Fig. 10. (Color online) Gap-midgap ratio ω_R as a function of the filling factor f for PCs with different substrate rotational angle in elliptic rods.

circular in shape. In these cases, the square rod PBG structures reveal the largest gap; the gap-midgap ratio is 36.2% at the conditions of $f = 0.16$ and an interference angle of 10° or 30° . The result is coincident with the parallelogram lattice, that is, the ω_R is similar at the same $\Delta\Phi$ when the interfered angle is 10° or 30° . The characteristics of realizable PBG structures are revealed in the simulation results tabulated in Table 2. The frequency at the middle of the gap ω_g is in units of $2\pi c/a$.

5. Conclusion

We utilized an interferometric lithographic system and double exposure method to theoretically and experimentally investigate PBG structures. Three types of lattice (square, triangular, and parallelogram) and four kinds of scatterer (square, circular, rectangular, and elliptical) with different sizes and lattice constants can be obtained with the interferometric lithographic system. The shape of the scatterers can vary from square to circular when $\Delta\Phi = 90^\circ$ and from rectangular to elliptical when $15^\circ \leq \Delta\Phi < 90^\circ$. Similar scatterers can be constructed experimentally. If the development processes are stable, the scatterer's shape may possibly be altered by controlling the development process. The lattice constants of the asymmetrically distorted 2D structure at $15^\circ \leq \Delta\Phi \leq 90^\circ$ are formulated from simulations of the isointensity surface. Square and triangular lattices are formed at $\Delta\Phi = 90^\circ$ and 60° , respectively. When $\Delta\Phi$ differs from 60° and 90° , the parallelogram lattice is obtained. The bandgap analysis shows that the PBGs of the periodic structures with the same substrate rotation angle and filling factor but different interference angles are similar. The maximum ω_R appears when the substrate rotation angle is 70° . The desired bandgap (with the largest frequency) width can be obtained from the correlation of ω_R and f . The above PBG structure results and the bandgap analysis are of great assistance in designing different forbidden

frequencies when lattice constants and scatterer shapes produced by the interferometric lithographic technique are well predicted.

The authors acknowledge the support of the National Science Council of Taiwan for this work through grants NSC-94-2623-7-008-006-AT and NSC-95-2221-E-008-138-MY3. The authors also acknowledge the assistance of Farn-Shiun Hwu of the Nanya Institute of Technology, Taiwan, for his assistance in the improvement of this manuscript.

References

1. X. Chen, Z. Zhang, S. R. J. Brueck, R. A. Carpio, and J. S. Petersen, "Process development for 180 nm structures using interferometric lithography and I-line photoresist," in *Emerging Lithographic Technologies*, D. E. Seeger, ed., Proc. SPIE **3048**, 309–318 (1997).
2. S. H. Zaidi and S. R. J. Brueck, "Multiple-exposure interferometric lithography," *J. Vac. Sci. Technol. B* **11**, 658–666 (1993).
3. N. D. Lai, W. P. Liang, J. H. Lin, and C. C. Hsu, "Rapid fabrication of large-area periodic structures containing well-defined defects by combining holography and mask techniques," *Opt. Express* **13**, 5331–5337 (2005).
4. E. J. Yablonovitch, "Photonic bandgap structures," *J. Opt. Soc. Am. B* **10**, 283–295 (1993).
5. S. Noda, K. Tomoda, N. Yamamoto, and A. Chutinan, "Full three-dimensional photonic bandgap crystals at near-infrared wavelengths," *Science* **289**, 604–606 (2000).
6. K. Srinivasan, P. E. Barclay, O. Painter, J. Chen, A. Y. Cho, and C. Gmachl, "Experimental demonstration of a high quality factor photonic crystal microcavity," *Appl. Phys. Lett.* **83**, 1915–1917 (2003).
7. K. S. L. Kenneth, B. Jose, B. K. T. Kenneth, C. Manish, A. J. A. Gehan, I. M. William, H. M. Gareth, and K. G. Karen, "Superhydrophobic carbon nanotube forests," *Nano Lett.* **3**, 1701–1705 (2003).
8. R. Furstner, W. Barthlott, C. Neinhuis, and P. Walzel, "Wetting and self-cleaning properties of artificial superhydrophobic surfaces," *Langmuir* **21**, 956–961 (2005).
9. R. Z. Wang, X. H. Wang, B. Y. Gu, and G. Z. Yang, "Effects of shapes and orientations of scatterers and lattice symmetries on the photonic bandgap in two-dimensional photonic crystals," *J. Appl. Phys.* **90**, 4307–4313 (2001).
10. W. M. Kuang, Z. L. Hou, and Y. Y. Liu, "The effects of shapes and symmetries of scatterers on the phononic bandgap in 2D phononic crystals," *Phys. Lett. A* **322**, 481–490 (2004).
11. C. C. Cheng and A. Scherer, "Fabrication of photonic bandgap crystals," *J. Vac. Sci. Technol. B* **13**, 2696–2700 (1995).
12. E. Chow, S. Y. Lin, and J. R. Wendt, "Quantitative analysis of bending efficiency in photonic crystal waveguide bends at $\lambda = 1.55 \mu\text{m}$ wavelengths," *Opt. Lett.* **26**, 286–288 (2001).
13. L. Pang, W. Nakagawa, and Y. Fainman, "Fabrication of two-dimensional photonic crystals with controlled defects by use of multiple exposures and direct write," *Appl. Opt.* **42**, 5450–5456 (2003).
14. F. Quiñónez, J. W. Menezes, L. Cescato, V. F. Rodriguez-Esquerre, H. Hernandez-Figueroa, and R. D. Mansano, "Bandgap of hexagonal 2D photonic crystals with elliptical holes recorded by interference lithography," *Opt. Express* **14**, 8578–8583 (2006).
15. J. W. Menezes, L. Cescato, E. J. de Carvalho, and E. S. Braga, "Recording different geometries of 2D hexagonal photonic crystals by choosing the phase between two-beam interference exposures," *Opt. Express* **14**, 4873–4879 (2006).
16. A. Fernandez and D. W. Phillion, "Effects of phase shifts on four-beam interference patterns," *Appl. Opt.* **37**, 473–478 (1998).
17. I. Mikulskas, J. Mickervicius, J. Vaitkus, R. Tomasiunas, V. Grigaliunas, V. Kopustinskas, and S. Meskinis, "Fabrication of photonic structures by means of interference lithography and reactive ion etching," *Appl. Surf. Sci.* **186**, 599–603 (2002).
18. H. H. Solak, C. David, J. Gobrecht, L. Wang, and F. Cerrina, "Multiple-beam interference lithography with electron beam written gratings," *J. Vac. Sci. Technol. B* **20**, 2844–2848 (2002).
19. C. W. Chien, J. C. Chen, and J. Y. Lee, "Applying an interferometric exposure model to analyze the influences of process parameters on the linewidth," *Appl. Opt.* **45**, 8278–8287 (2006).
20. K. M. Leung and Y. F. Liu, "Large complete bandgap in two-dimensional photonic crystals with elliptic air holes," *Phys. Rev. B* **60**, 10610–10612 (1990).
21. M. Ho, C. T. Chan, and C. M. Soukoulis, "Existence of a photonic gap in periodic dielectric structures," *Phys. Rev. Lett.* **65**, 3152–3155 (1990).
22. S. Johnson and J. Joannopoulos, "Block-iterative frequency-domain methods for Maxwell's equations in a planewave basis," *Opt. Express* **8**, 173–190 (2001).
23. X. L. Yang, L. Z. Cai, and Q. Liu, "Theoretical bandgap modeling of two-dimensional triangular photonic crystals formed by interference technique of three noncoplanar beams," *Opt. Express* **11**, 1050–1055 (2003).
24. B. A. Mello, I. F. Costa, L. Cescato, and C. R. A. Lima, "Developed profile of holographically exposed photoresist gratings," *Appl. Opt.* **34**, 597–603 (1995).
25. A. I. Cabuz, E. Centeno, and D. Cassagne, "Superprism effect in bidimensional rectangular photonic crystal," *Appl. Phys. Lett.* **84**, 2031–2033 (2004).
26. J. D. Joannopoulos, R. D. Mead, and J. N. Winn, *Photonic Crystals* (Princeton U. Press, 1995).
27. O. Toader, T. Y. M. Chan, and S. John, "Photonic bandgap architectures for holographic lithography," *Phys. Rev. Lett.* **92**, 043905-1–043905-4 (2004).